A nanoporous, ultrahydrophobic aluminum-coating process with exceptional dropwise condensation and shedding properties

Lance Brockway[1,2,+] and Hayden Taylor[1,2,*]

[1] Department of Mechanical Engineering,
6159 Etcheverry Hall, University of California, Berkeley, CA 94720

[2] Berkeley Education Alliance for Research in Singapore (BEARS)
CREATE Tower, 1 Create Way, #11-00 Singapore 138602

*Corresponding author – telephone: +1 510 642-4901; e-mail: hkt@berkeley.edu

[+] Now with Nelumbo, Inc.

Keywords: Superhydrophobic, oleophobic, zinc oxide, ZnO, re-entrant

Abstract

Many studies have shown that dropwise condensation can enhance air-side heat transfer coefficients by at least an order of magnitude relative to filmwise condensation. However, among the hundreds of superhydrophobic surface-modification processes previously reported, there remains a lack of coating methods that enable stable dropwise condensation and can be applied to aluminum — by far the most common material for the air side of heat exchangers, *e.g.* in air conditioning. Here we present a bottom-up synthesis technique to grow zinc oxide-based films on to aluminum with tunable nanoporosity and strongly re-entrant surface features. These surfaces exhibit exceptional static water contact angles of up to 178° with a hysteresis less than 3° and a slide angle of 1°. We have further characterized the surfaces in the presence of six different liquids, and show that our optimal surface can repel even dipropylene glycol with a contact angle of 124°, even though its surface tension is less than half that of water. Crucially, we have also tested our films under water-condensing conditions in flowing air, characterizing the droplet-shedding behavior, and we have understood how to tune the growth process to deliver stable droplet-shedding instead of flooding. The process uses inexpensive reagents, can operate below 100 °C via immersion in an aqueous bath, and takes 1–3 hours to complete, making it readily scalable to areas of many square meters and complex geometries.

1. Introduction

Dropwise condensation has been well established to enhance condensation heat transfer coefficients by an order of magnitude or more relative to filmwise condensation [1]–[5]. A requirement for highly effective dropwise condensation is a superhydrophobic heat transfer surface, the two common ingredients of which are a roughened texture and a low surface energy [6]. Countless processing routes have been demonstrated to achieve superhydrophobic behavior on metals, polymers and ceramics [6]. Only a small subset of potential superhydrophobic surfaces, however, is suitable for use under condensing conditions, because the surface needs to conduct heat rapidly away from condensing droplets [3], [4], [7] while still enabling droplets to shed as they grow and coalesce [8]–[14].

1.1. The need for superhydrophobic coatings in air conditioning systems

One application in which dropwise condensation could potentially reduce energy consumption is on the air side of evaporator coils in air conditioning systems. Air conditioning currently accounts for about 6% of U.S. electricity consumption [15], and for up to 20% in tropical countries such as Singapore [16]. Enhanced, dropwise heat transfer at air-cooling surfaces [2], [17] would enable higher coolant temperatures to be used for a given heat flux, and hence higher coefficients of performance to be attained. Moreover, the absence of a water film on cooling surfaces would result in less impedance to air flow in parallel-plate heat exchanger configurations [5], [18], which are ubiquitous. Thirdly, eliminating stagnant water would reduce the risk of fungal or bacterial growth inside a heat exchanger [19], and retard metal corrosion [5].

Nevertheless, evaporator coils today are predominantly given *hydrophilic* surface treatments [18] which promote filmwise condensation, on the ground that conventional, moderately hydrophobic coatings shed their droplets only under gravitational action, so that droplets would first need to reach a diameter comparable to water's capillary length in air (~2 mm). This distance is similar to the gap between the parallel plates, or 'fins', of most heat exchangers, which is constrained by heat transfer requirements. Thus, droplets growing towards their capillary length would frequently bridge fin gaps and impede air flow even more severely than in the filmwise condensation mode.

For dropwise condensation to be feasible in an evaporator coil, the shedding diameters of droplets need to be reduced to less than about half the spacing of the fins. In additional to gravitational shedding, droplets might be removed by the aerodynamic forces of the flowing air [20], or by coalescence-induced jumping whereby liberated surface energy is converted to kinetic energy [4], [9], [21]. For either of these alternative shedding modes to play a role, the adhesion between growing droplets and the heat transfer surface must be reduced, meaning that the contact area must be minimized while still providing an adequate heat conduction path. Additionally, if droplet shedding into the air is promoted, a means of capturing and extracting the droplets from the airstream needs to be devised.

1.2. Engineering droplet-shedding mechanisms

It has been argued by Miljkovic [7] that condensation heat transfer is maximized when growing droplets remain in a partial-wetting state, whereby only a small portion of the base of the droplet wets the rough underlying surface. This mode is predicted to occur when it is energetically favorable for a droplet expanding from a wetted location to remain clear of the surrounding solid surface and not wet the adjacent features [9]. The partial-wetting situation is expected when [3], [8]:

$$E^* = \frac{\cos\theta_a^{CB}}{\cos\theta_a^{W}} = \frac{-1}{r\cos\theta_a} < 1, \tag{1}$$

where θ_a^{CB}, θ_a^{W}, and θ_a are the advancing contact angles for droplets in the Cassie–Baxter state, in the Wenzel state, and on a smooth flat surface, respectively. The roughness, *r*, is defined as the ratio of the actual surface area to the projected area of the substrate [10].

The alternatives to partial wetting are a fully wetted (Wenzel [22]) mode and a completely "suspended" (effectively Cassie–Baxter (CB) [23]) state in which no surface pores are wet. The partial-wetting mode has been measured to yield condensation heat transfer coefficients around six times higher than in a suspended state [23], and about 30% higher than the Wenzel state [24].

Surfaces that do not have a low enough surface energy or great enough roughness will tend to enter the Wenzel state. Those with particularly high roughness and/or low surface energy may enter the suspended state, especially if the surface energy is patterned to promote condensation at the tips of the surface's asperities rather than within its pores [11], [25]. It has also been suggested that the geometry can be controlled by tapering surface protrusions to induce dewetting transitions during condensation [12].

In addition, Miljkovic has suggested that to inhibit flooding of a surface during condensation, the mean separation of the nucleated droplets should lie between two and five times the pitch of the structures on the substrate [7]. The nucleation density depends on the supersaturation of air at the surface, as well as on the presence of any disruptions to the hydrophobic chemistry of the surface.

1.3. Processing routes to achieve partial-wetting superhydrophobicity

The question therefore arises of how to produce a surface that combines sufficient roughness and low surface energy, while offering adequate thermal conductance and a large enough spacing of nucleation sites under condensing conditions to inhibit surface flooding. Air conditioning heat exchangers are almost exclusively manufactured from fins of aluminum alloy sheet less than 0.2 mm thick, mounted on coolant-carrying pipes made of either copper or aluminum alloys. Coalescence-induced droplet jumping has been demonstrated from a nanostructured, copper oxide surface with a hydrophobic surface termination [26]. In contrast, while there have been many reports of superhydrophobic modifications of aluminum surfaces, there is a dearth of experimentation to show whether those surfaces operate effectively under condensing conditions at atmospheric pressure. Instead, characterization has often been limited to the measurement of sessile, advancing and receding contact angles, as well as the sliding or roll-off angles of droplets. Such results, while enabling rapid screening of candidate processes, do not conclusively establish suitability for dropwise condensation.

1.3.1. Direct structuring of the metal surface

One approach to raising the roughness of a metallic surface is to create periodic micro- or nano-scale topographies. This has been done through photolithographic and etching processes (*e.g.* [27]–[29]), which offer nanometer-level precision but require smooth, flat starting surfaces and multiple process steps, in some cases including energy-intensive plasma-based processing under vacuum. Alternatively, and more scalably, features with dimensions as small as ~30 μm have been mechanically embossed into aluminum alloy surfaces [30], [31].

Controlled surface patterning can serve a purpose beyond increasing roughness. Microscopic grooves aligned perpendicular to the air flow have been shown to promote the gravitational removal of condensate and reduce 'carryover' of condensate into the downstream air [5]. Specific surface topographies, including shark-skin mimics composed of arrays of aligned sub-micron grooves, have been shown to serve an antibacterial function [32], which could further benefit evaporator coil surfaces.

One particularly desirable attribute in a superhydrophobic surface is a *re-entrant* pore morphology, which helps to direct the surface tension of a suspended liquid out of the pores, increasing resilience to wetting [33]. Lithography followed by an undercutting etch process has been used to create model re-entrant

geometries for studying liquid behavior [34], [35], but these approaches seem unlikely to be scalable. There is no obvious way for direct embossing to produce a re-entrant structure because the stamp has to be subsequently retracted from the deformed material. The use of woven metal meshes is one potentially scalable way to obtain geometrically regular, re-entrant structures [36].

1.3.2. Bottom-up modification of the metal surface

The need to produce re-entrant features over large areas has therefore led to the development of surface treatment processes in which micro- and nano-scale structures emerge, with limited spatial order, during a chemical reaction. Here we specifically address treatments for aluminum and its alloys.

Hydrothermal treatments of many kinds have been reported, the simplest of which involves exposing a bare aluminum surface to hot (*e.g.* ~70 °C) deionized water, and has been shown by He *et al*. [37] to result in a randomly arranged structure, with pores < 100 nm in size. Immersion in sodium hydroxide solution has also been used [38]–[40], with reported contact angles (CAs) after surface termination as high as 170° and hysteresis as low as 3–5° [39].

Anodization can also be controlled to yield nanoscopic pores which increase surface roughness [41]–[46]. Anodization has been performed in sulfuric acid [43], citric acid [44], oxalic acid [42], and sodium chloride [45] baths, resulting in differing pore morphologies. Anodization has been combined by Yin *et al*. with wet etching and fluorosilane surface termination to yield a contact angle of 168° and a slide angle of 5° [43]. Jenner *et al.* also used etching to turn vertical-sidewalled pores into tapered spikes, reducing the solid fraction in contact with the droplet and yielding a sessile CA of 161° and a rolling angle, after fluoropolymer treatment, well below 1° [44].

1.3.3. Deposition of ceramic films

Adding a film of a second material, as opposed to roughening or oxidizing the base metal, may offer greater control of surface geometries. In particular, processes for growing zinc oxide nanostructures from solution have been extensively developed, and ZnO offers a thermal conductivity between 35 $Wm^{-1}K^{-1}$ [47] and 100 $Wm^{-1}K^{-1}$ [48], which is slightly superior to that of alumina, albeit 4–10 times lower than metallic aluminum.

ZnO with a high roughness suitable for liquid-repellent surfaces has been produced in the form of nanowires [49], nanoparticles [50], and porous films, often via immersion of a target substrate into, for example, a solution of zinc acetate dehydrate in acetone [51], an aqueous solution of zinc nitrate, ammonium chloride, urea and ammonia [52] (for an advancing CA of up to 158°), or an aqueous solution of zinc nitrate hexahydrate and hexamethylenetetramine [53]. Spray pyrolysis of aqueous zinc acetate has also been employed [54], removing the need for immersion but requiring a much higher temperature and a direct line of sight from the source of the spray to the target surface. Most of these reports do not stress a particular need for a specific substrate material; nor do the processes require a catalyst. However, Yao, who deposits ‘nanoflakes’ of ZnO on to aluminum [53], does argue that the aluminum substrate plays a vital role in aligning the growth of the nanoflakes to be approximately perpendicular to the substrate surface, and for directing flakes to form as opposed to nanowires, as would be obtained on a crystalline silicon substrate.

Alternative potential methods of ZnO deposition, including sputtering and electrochemical techniques, are less appealing in that they may require vacuum processing, impose special requirements on the electrical conductance of the substrate, or produce films that are too smooth to enhance liquid repellence. Other materials including titania [55] and zeolites [56] have also been explored for roughening surfaces at the nanoscale.

Another very promising option is to create rare earth oxide films, which have been shown to be naturally hydrophobic [57], removing the need for a separate surface termination step. Open questions are whether the required source materials could be obtained at an affordable cost to be used in industrial applications such as air conditioning, and whether suitable solution-based processes can be found to create films of these oxides with nano-scale roughness.

Carbon nanostructures composed of nanotube (CNT) forests or crumpled graphene have been widely explored and offer high thermal conductance [58]. The extremely low solid area fraction of a nanotube forest means that, in a composite wetting state, contact angles can reach well above 170°. These materials may offer low cost, although the chemical vapor deposition of CNTs or graphene requires vacuum processing. Solution-based exfoliation and deposition of graphene or graphene oxide may be more scalable.

1.3.4. Surface termination protocols

Because alumina, zinc oxide and most other oxides are strongly hydrophilic, almost all of the methods surveyed above need to be combined with a hydrophobic surface termination step. While it is well known that hydrophobic composite droplet contact modes can exist on structured surfaces with hydrophilic chemistry (*e.g.* [59]), we are concerned here with dropwise condensation, for which previous reports suggest that hydrophobic chemistry is indeed needed.

The predominant approach is to terminate the surface with a highly fluorinated molecule, such as a fluorosilane, by exposing it to a vapor or immersing it in, *e.g.*, a solution of the molecule in ethanol. Molecules commonly used have included 1H,1H,2H,2H-Perfluorooctyltriethoxysilane [8], [39], 1H,1H,2H,2H-Perfluorodecyltrimethoxysilane [37], and 1H,1H,2H,2H-Perfluorooctyltrichlorosilane [4]. Non-fluorinated silanes such as trichloro(octadecyl)silane [8] and dichlorodimethylsilane [8] have also been used. An alternative family of treatments involves immersion in an acidic solution, for example oleic [45] or stearic acid [53], [60]. In some cases it is possible to combine the surface texturing and surface termination steps. For example, electrochemical etching of copper in ethanolic stearic acid has been used to produce a rough surface and simultaneously terminate the surface hydrophobically [61].

None of these hydrophobization methods can be expected to produce flawless surfaces and so the reported performance of any given process will inevitably depend not only on the morphology of the modified surface, but on the specifics of the termination process. In particular, the binding of fluorosilane molecules is not guaranteed to result in a perfect self-assembled monolayer; polymerization of the molecule and substantial thickening of surface nanostructures can occur [4]. Moreover, there is a lack of experimental data on the longevity of these various termination methods in service, and on their resilience to mechanical abrasion.

1.3.5. Non-specific deposition of polymer and composite films

Apart from the array of metallic and ceramic surfaces described above, there have been thousands of reports of polymer-based superhydrophobic coatings produced, by, *e.g.*, spray or electrospinning [62], mechanical extrusion [63], controlled solvent evaporation [64], or phase separation [65]. Such coatings frequently incorporate nanoparticles, *e.g.*, of silica, to enhance roughness. While these materials have many potential applications, very few of them are likely to lie in heat transfer. Polymers, as well as having thermal conductivities two orders of magnitude lower than ceramics such as alumina or zinc oxide, are typically deposited in far thicker layers than a grown oxide film: many micrometers as opposed to a few micrometers or less. Polymeric coatings, therefore, would defeat the purpose of eliminating an insulating water film from the heat transfer surface. Liquid-infused porous surfaces can add a similarly problematic thermal impedance [66].

1.3.6. Multi-scale surfaces

Bottom-up nanostructure creation has been widely coupled with top-down microstructures, to yield multi-scale surfaces which mimic the exceptional water-repellence of biological structures such as the lotus leaf (*e.g.* [14], [67]). Such structures minimize solid–liquid contact area and maximize robustness against wetting, and it has been suggested that microstructure tapering may help to expel condensing droplets from a surface [68].

1.4. A new, high-performance coating procedure for aluminum

Here, we report an exceptionally simple, safe, and rapid technique for growing a superhydrophobic ZnO coating directly on to aluminum, yielding higher sessile contact angles, after surface silanization, than any others that we have seen reported. Compared to the closest comparable process in the literature for depositing ZnO on Al [53], we report much higher water contact angle (178° *cf.* 157°) and a far lower sliding angle (1° *cf.* 8°). Our surface demonstrates stable dropwise condensation at a supersaturation of $1.50^{+0.20}_{-0.15}$, with droplets shedding from the surface in moving air at a small fraction of the capillary length.

2. Materials and Methods

2.1. Porous zinc oxide synthesis

Porous zinc oxide coatings were synthesized by immersing aluminum scanning electron microscopy sample-mounting pegs into equimolar aqueous solutions of zinc nitrate and hexamine [33]. Reactions were performed with concentrations of 10 mM to 100 mM and temperatures of 70 °C to 110 °C for 90 minutes. At 110 °C a sealed container was used (reaction pressure ~1.4 bar); at lower temperatures the reaction was at atmospheric pressure. The coated aluminum substrates were then removed from the bath, rinsed with deionized water, and allowed to air-dry.

2.2. Silanization of surfaces

Prior to modifying the zinc oxide coated aluminum substrates with hydrophobic silanes, the substrates were cleaned to remove reaction byproducts in an oxygen plasma (60 W, 200 mTorr, 2 min). The substrates were then immediately placed in a vacuum desiccator with 100 µL of the perfluorosilane (1H,1H,2H,2H-Perfluorooctyltrichlorosilane, Sigma Aldrich). The desiccator was then pumped for 20 minutes to vaporize the silane followed by letting it settle for 40 minutes before venting the chamber. Upon removal, the substrates were rinsed with deionized water to remove unreacted perfluorosilane, dried, and finally annealed at 120 °C for one hour on a hot plate.

2.3. Characterization

The coatings were imaged using scanning electron microscopy (SEM) at 20 kV with a secondary electron detector and characterized for phase using X-ray diffraction (XRD, Bragg-Brentano powder diffractometer) with Cu K-α radiation.

Contact angle measurements were performed using the sessile-drop technique with a 5.5 µL droplet of one of six test liquids detailed in the results below. Droplets were imaged from the side with a 4X objective (Olympus Plan Achromat), a 30 mm focal-length achromatic doublet (Thorlabs, Newton, NJ), and a CMOS image sensor (Thorlabs DCC1645C) [33]. Contact angle hysteresis was determined by mounting the samples on a stage that was manually tilted at a rate of 0.25 $°s^{-1}$ while imaging a static droplet. The advancing and receding contact angles were measured from the final video frame captured before droplet motion began. Hysteresis is simply defined as the difference between advancing and

receding angles. Sessile-drop contact angles were estimated by fitting the Young–Laplace equation to the image data (LBADSA) [69] and droplets on the verge of moving were analyzed with B-spline active contours (Dropsnake) [70]. Sessile-drop contact angles were extracted for ten separate droplets per sample; hysteresis was measured for five droplets per sample.

Measurements of droplet-shedding performance under condensing conditions were collected using a custom-built wind tunnel with a cold plate for sample-mounting. Details of the apparatus are given in the Supplementary Information (SI). For these measurements, the substrates were cooled to 15±0.5 °C and exposed to an air flow at 40±0.5 ˚C, 35±2 % relative humidity, and a velocity of 10±0.25ms^{-1}. Video images of the condensation and droplet-shedding process were recorded over periods exceeding 10 minutes, using a stereomicroscope (Amscope, SM zoom trinocular) with a long-working-distance 4.5X objective connected to a CMOS image sensor (Thorlabs DCC1645C).

3. Results and Discussion

3.1. Coating morphologies

Figure 1 shows scanning electron micrographs of the porous zinc oxide surfaces for a range of reactant concentrations and bath temperatures. As reactant concentration increases for a given bath temperature, the pore size appears to decrease. Pore sizes range from below 100 nm to larger than 3 μm while the film thickness, as measured by SEM cross-sectioning, varies from 500 nm to 3 μm across the array of reaction conditions. X-ray diffraction analysis (see SI) indicates the formation of wurtzite zinc oxide using this synthesis technique. This ZnO phase has a high thermal conductivity ranging from 100 Wm^{-1}K^{-1} for single crystalline conduction pathways [48] down to 35 Wm^{-1}K^{-1} for nanograined materials [47] at room temperature. Given a 1 μm-thick smooth ZnO film grown directly on standard 125 μm-thick aluminum fin stock, the thermal resistance increase upon application is less than 4% relative to the bare fin stock. For comparison, a film of water 120 μm thick [71] would increase the thermal resistance of a bare aluminum fin 100-fold. Meanwhile, a 1 μm-thick polymer coating would increase the thermal resistance of a fin 10-fold. The ZnO coating can therefore greatly improve overall thermal conductance relative to conventional, filmwise condensation and without having the detrimental effects on performance of a polymer film.

3.2. Sessile water droplet contact angles and hysteresis

Observations of the sessile-drop water contact angle (Figure 2a) and contact angle hysteresis (Figure 2b) show that contact angle is at its highest (177°) and hysteresis is simultaneously at its lowest (3°) for a reaction temperature of 110 °C and reactant concentrations of 75 mM after a 90-minute growth time. Surfaces produced at 110 °C with reactant concentrations lower than 75 mM have larger pores, as observed in the SEM images, while at 100 mM the reaction appears to have progressed to such an extent that some of the pores have closed in upon themselves. Similar trends are seen for growth temperatures of 70 °C and 90 °C, with sessile contact angle peaking and hysteresis simultaneously showing a minimum at growth conditions of 70 °C/50 mM and 90 °C/75 mM.

Even though there is a non-monotonic relationship between reactant concentrations and the measured variables of sessile-drop contact angle and hysteresis, Figure 2c indicates a clear negative linear correlation between sessile-drop contact angle and hysteresis that applies across all reaction conditions. The correlation implies that for every 1° gained in sessile-drop contact angle, hysteresis reduces by 1.18° on average, and extrapolates towards negligible hysteresis at a hypothetical contact angle of 180°.

This negative correlation between hysteresis and contact angle implies that all samples, when measured using the sessile-drop technique, remain approximately in a Cassie–Baxter state — the condition in which

the droplet sits on top of the structures with air pockets retained inside surface recesses. Under these conditions, a higher apparent contact angle reduces both the liquid–solid contact area and the length of features' perimeters in contact with liquid. A positive correlation between hysteresis and contact angle in Figure 2c would have implied that droplets were completely filling the pores and therefore in a Wenzel state [72]. We compare our observed values with the model of McHale [72] linking hysteresis to sessile-drop contact angle for the Cassie–Baxter mode (see SI), and find that our observed hysteresis values are around 2.5 times higher than McHale's model predicts. This difference could arise from the filling of a small fraction of pores beneath the droplet, giving a hysteresis higher than would be expected in a purely CB state.

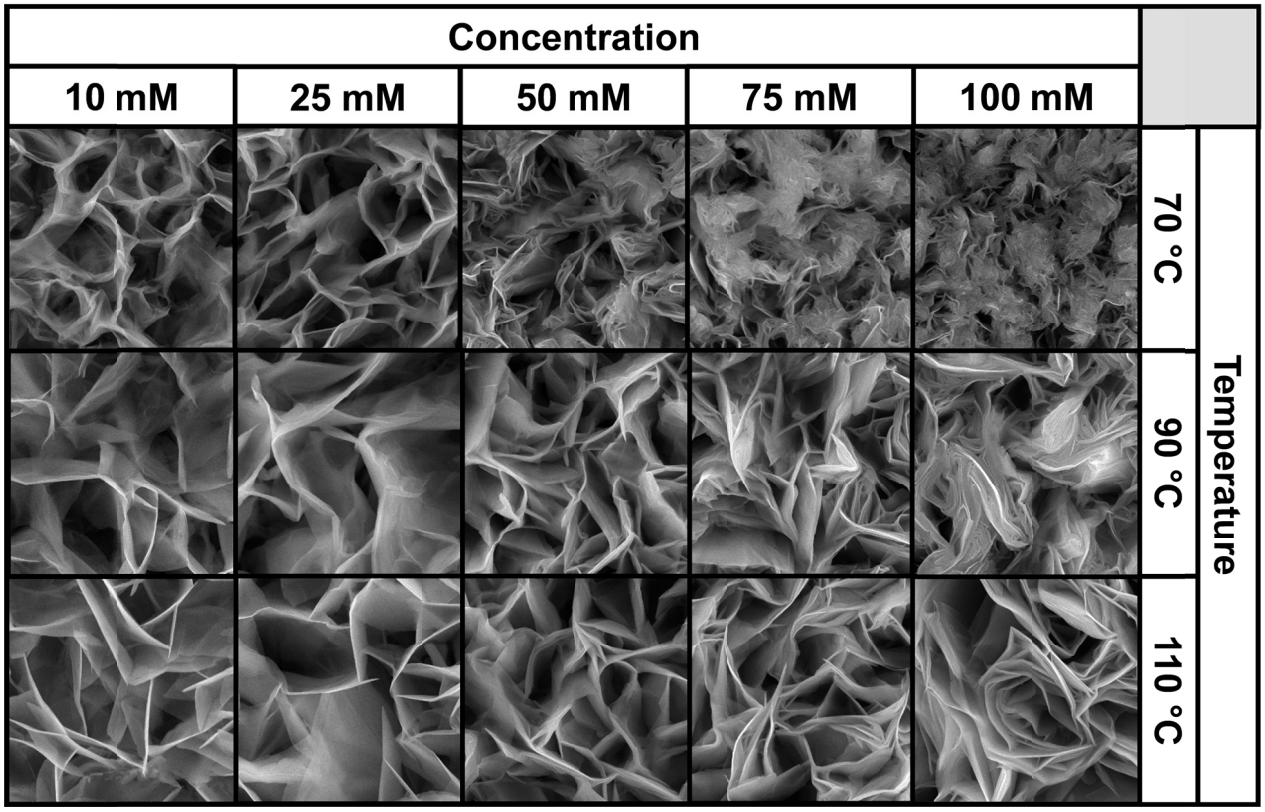

Figure 1. Scanning electron micrograph of a coated aluminum surface indicating that the surface properties are tunable by varying the concentration and temperature of the reaction bath. Each frame in the figure is 6.5 µm in width. Pore diameter across this array of reaction conditions ranges from below 100 nm to above 3 µm. Processing time was 90 minutes.

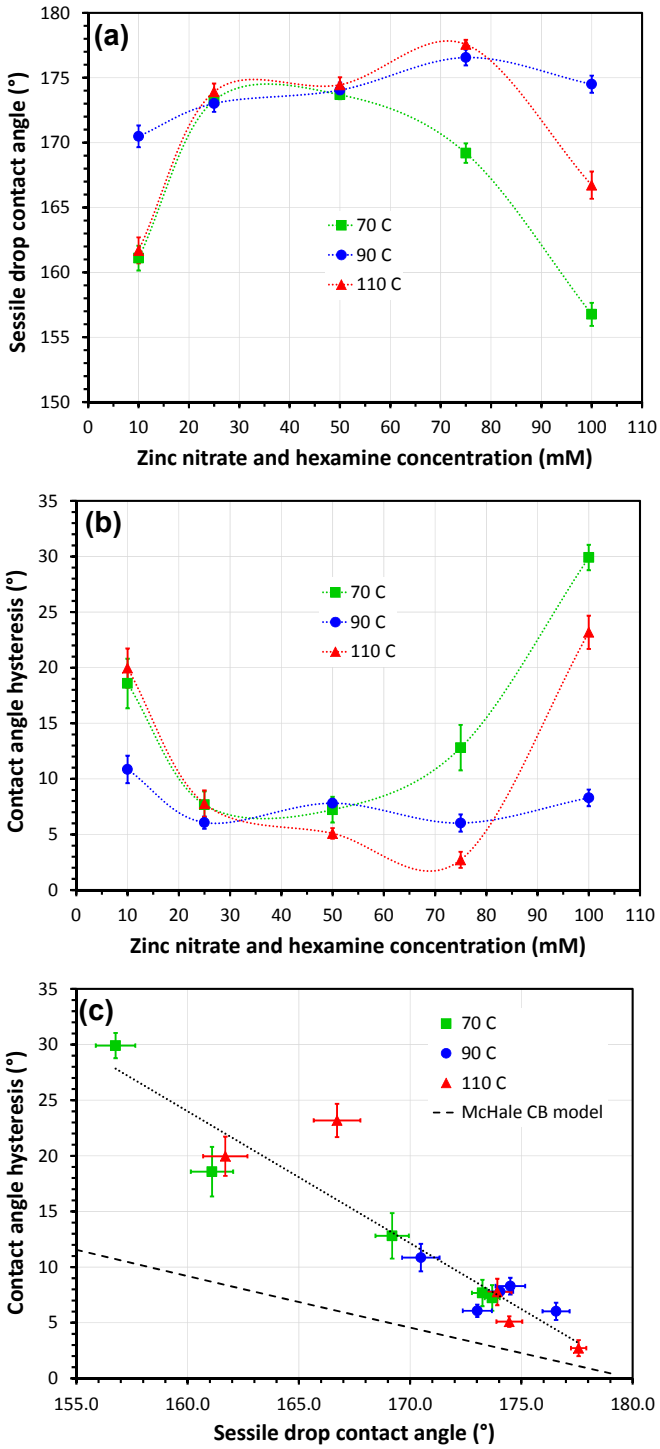

Figure 2. (a) Plot of the water sessile drop contact angle versus reaction conditions. (b) Plot of contact angle hysteresis versus reaction conditions. (c) Plot of sessile drop contact angle versus contact angle hysteresis, indicating a strong linear correlation independent of reaction conditions for these porous ZnO structures. In (a) and (b), the dotted lines are to guide the eye. In (c), the best-fit straight line has a gradient of –1.18. For all plots, error bars represent ± one standard error of the mean. In the case of sessile droplet contact angles, sample size is ten separate droplets per specimen; for hysteresis, sample size is five droplets per specimen.

3.3. Modeling of pore geometry distributions

To characterize the surfaces further, we have applied our previously reported method for modeling heterogeneous porous surfaces [33]. Briefly, our modeling approach accounts for heterogeneity of pore shapes (*e.g.* Figure 3a–d) by modeling the surface as an array of pores with re-entrant angles Ψ that follow an approximately Gaussian distribution with mean Ψ_0 and standard deviation σ_0. Pores with $\Psi < \theta_0$ will remain empty (Figure 3e) while those with $\Psi > \theta_0$ will fill (Figure 3g). Thus, for any particular liquid, a fraction $0 \leq \phi_f \leq 1$ of the pores within the liquid-covered area will be filled. Pores are modeled as having an internal surface roughness of *r*, and a fraction ϕ_T of the projected area of the surface is considered to be outside of the pores and always in contact with the liquid. From these assumptions follow a generalized Cassie–Baxter model:

$$\cos\theta^* = \phi_T \cos\theta_0 + (1-\phi_T)\left[\phi_f\, r \cos\theta_0 - (1-\phi_f)\right] \tag{2}$$

By measuring the apparent contact angles θ^* of multiple liquids on a given porous surface, and the contact angle θ_0 on a smooth surface with equivalent chemistry, the four fitting parameters of Ψ_0, σ_0, ϕ_T and *r* can be extracted, with ϕ_f following from Ψ_0, σ_0 and θ_0 via the assumed Gaussian distribution.

We use this modeling approach to characterize zinc oxide surfaces produced with three particular sets of process conditions. Process and extracted model parameters are shown in Table 1, and the fitted models are illustrated together with the measured data on a plot of $\cos\theta^*$ against $\cos\theta_0$ in Figure 4a. Surfaces were probed with a variety of test liquids with surface tensions ranging from 22.7 mNm^{-1} (methanol) to 72.8 mNm^{-1} (water). Of the three surfaces characterized, Process A (25 mM, 70 ˚C) yields the most liquid-repellent behavior overall, giving a contact angle well in excess of 90° for dipropylene glycol, whose surface tension is less than half that of water. As expected, the extracted average re-entrant angle of $\Psi_0 = 51.0°$ is the most strongly re-entrant of the three surfaces.

Table 1. Mean re-entrant angle (Ψ_0), reentrant angle standard deviation (σ_0), surface roughness (r), and solid fraction of the nanostructures' tips (ϕ_T) fit for three samples included in this study. *E is computed using Equation 1.**

	ZnO growth conditions	Ψ_0	σ_0	*r*	ϕ_T	*E** (water)
Process A	25 mM, 70 ˚C	51.0˚	25.0˚	3.50	0.0051	0.138
Process B	50 mM, 110 ˚C	57.1˚	29.6˚	3.59	0.0066	0.135
Process C	100 mM, 70 ˚C	76.2˚	66.6˚	3.67	0.1080	0.132

Figure 4b is a plot of the sessile drop contact angle versus reaction conditions for one particular probe liquid: 700 g/mol poly(ethylene glycol) diacrylate (PEGDA-700). This plot shows lower contact angles and different optimal processing conditions compared to water on the same surfaces (Figure 2a) because PEGDA-700 has a lower surface tension than water and penetrates more extensively into the pores. Figure 4b indicates that the sample synthesized at 70 °C and 25 mM offers the highest sessile contact angle for PEGDA-700.

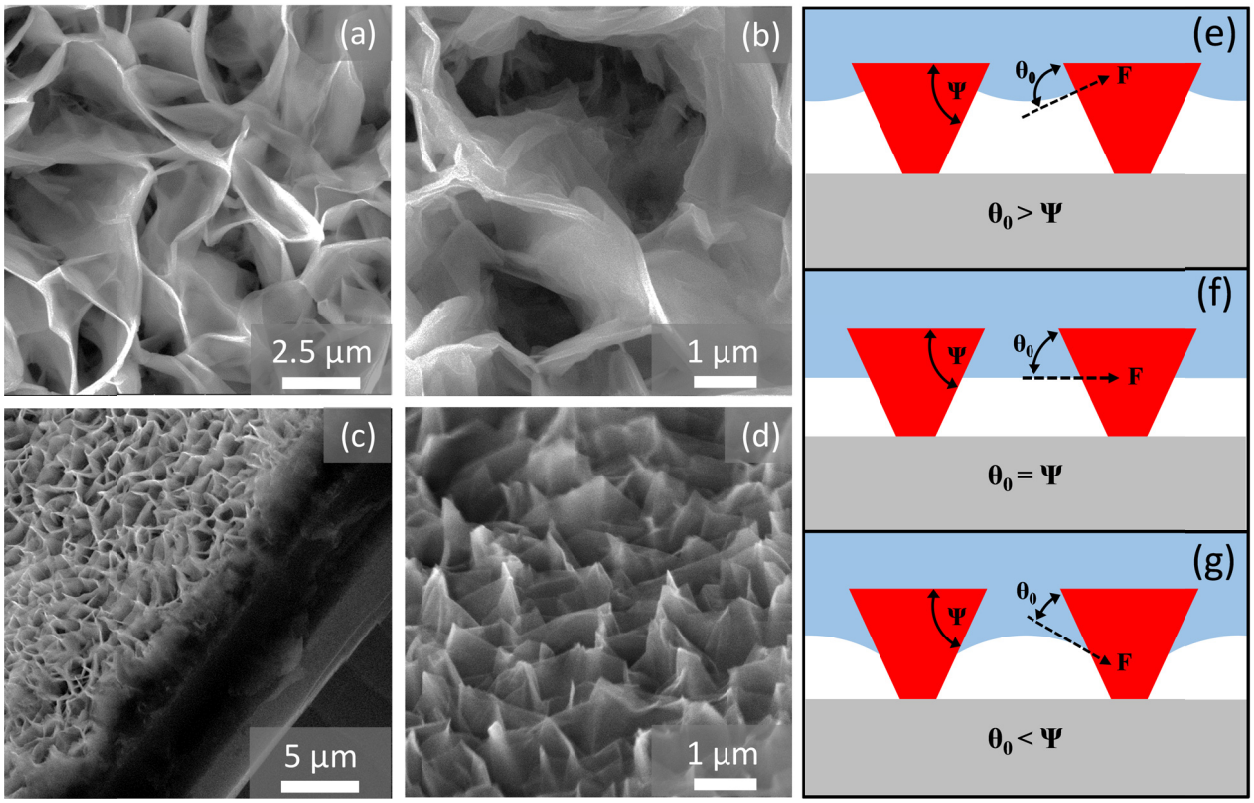

Figure 3. Scanning electron micrographs of the porous zinc oxide films showing the pore depth profile and re-entrant surface geometries (a) & (b) from a sky view of the surface, (c) 45° to the surface, and (d) 75° from the vertical. The pores do not go straight down to the aluminum surface. Instead, they wind through the coatings at varying angles. Process conditions were (a) 25 mM, 90 °C, (b)–(d) 25 mM, 70 °C. In an idealization of the geometry of a single pore, a re-entrant structure can support a composite interface if (e) $\theta_0 > \Psi$. The net force acting on the droplet will become zero at (f) $\theta_0 = \Psi$ and be into the pore when (g) $\theta_0 < \Psi$, resulting in a break-down of the composite interface and complete wetting.

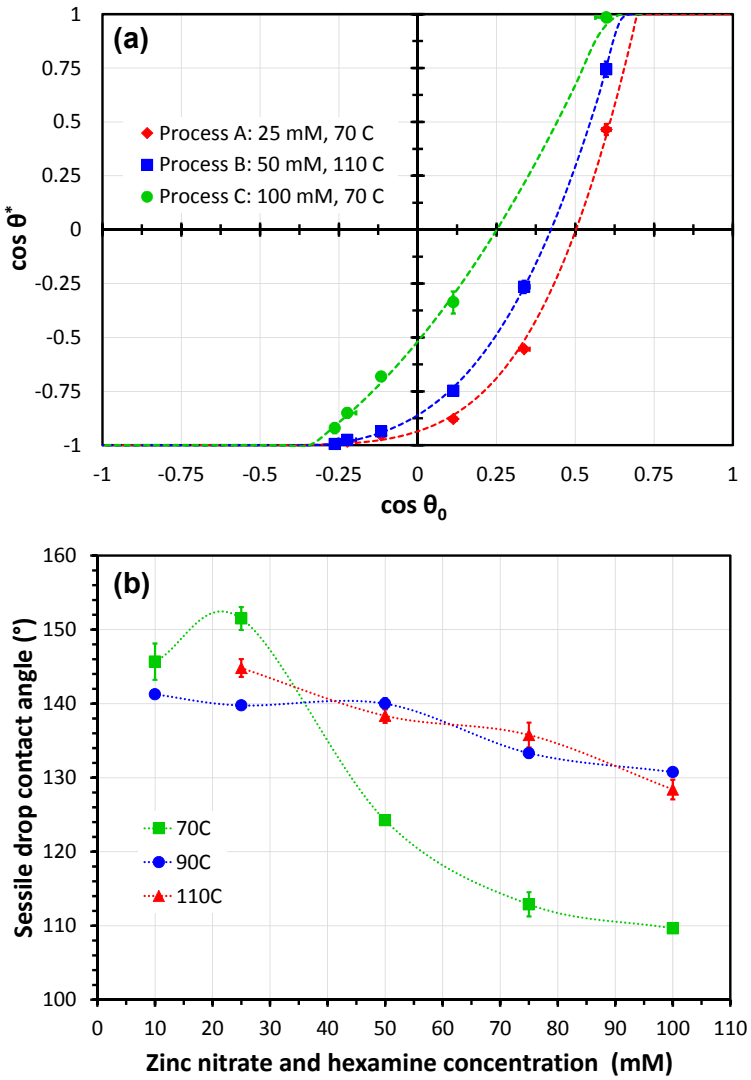

Figure 4. (a) Plot of the cosine of the contact angle on a smooth surface (θ_0) versus the cosine of the apparent contact angle on the porous ZnO surface (θ^*) for various test liquids. This shows that the optimal surface can remain in Cassie–Baxter wetting mode with a wide range of materials such as water (γ = 72.8 mN/m) [73], glycerol (γ = 64 mN/m) [73], thiodiglycol (54 mN/m) [73], PEGDA-700 (γ = 42.3 mN/m) [74], dipropylene glycol (33.9 mN/m) [73], and methanol (γ = 22.7 mN/m) [73]. The dotted lines show the model fit to determine the surface properties. (b) Sessile drop contact angle for PEGDA-700 (γ = 42.3 mN/m) [74] versus reaction conditions (90-minute reaction time). Note that the 10 mM, 110 °C case gives a very low contact angle which is out of the range of the scale (see SI for numerical data). The dotted lines are to guide the eye. Error bars for both figures are one standard error of the mean based on five separate droplet measurements per specimen. In several cases, error bars are smaller than symbols used.

3.4. Water droplet roll-off angles

The substrate tilting angle at which a sessile droplet begins to roll or slide across a surface (the 'roll-off' angle) may provide an indication of the ability of a surface to shed condensate. The roll-off angle is correlated with the contact angle hysteresis because, in order to move, the droplet's shape is deformed until the advancing contact angle is reached on one side of the droplet and the receding angle on the other.

Tilting the substrate exerts a gravitational force to provide this deformation. We have characterized the roll-off angle of the surface grown with Process B (110 °C and 50 mM) by capturing a video of a 5.5 µL droplet beginning to roll across the surface. A roll-off angle of 1° was recorded and a sequence of frames is shown in Figure 5. Since we could not distinguish visually between rolling and sliding, we use the term 'roll-off angle' to encompass both possibilities.

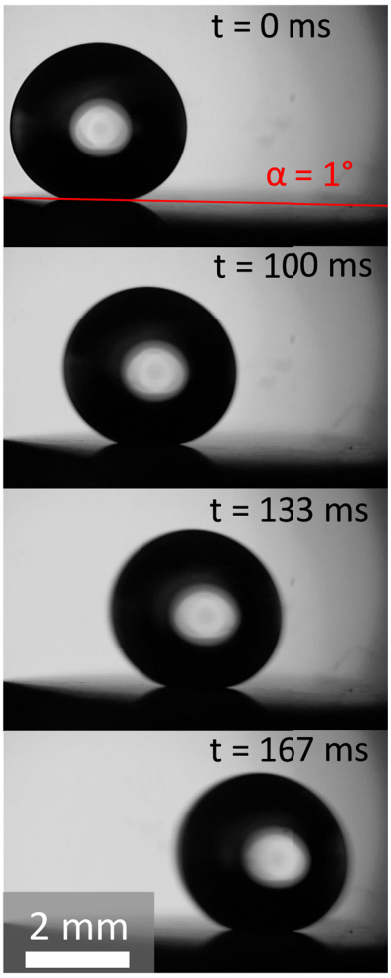

Figure 5. Time-lapse image of a droplet rolling or sliding off the porous zinc oxide structure surface synthesized with Process B (110 °C and 50 mM). This sample has an average water contact angle, hysteresis, and slide angle of 175°, 5°, and 1° respectively.

We can interpret roll-off angle using the following expression proposed by Lv for the lateral adhesive force F_{ad} between the droplet and the solid surface [75]:

$$F_{ad} = 2R\gamma(1 + \cos\theta_0)\sqrt{\phi_T} = \rho V g \sin\alpha, \quad (3)$$

where R is the mean radius of the contact line, γ is the surface tension of water, θ_0 is the contact angle on a smooth surface, ϕ_T is the wetting solid fraction, ρ is the density of water, V is the volume of the droplet, g is the acceleration due to gravity, and α is the roll-off angle.

Taking $\phi_T = 0.0066$ from our model calibration above and computing R = 110 μm based on an apparent contact angle of 174.4° and V = 5.5 μL (see SI for details) leads to a predicted adhesion force of 920 nN and hence a roll-off angle of 0.98°, agreeing with the roll-off angle of 1° independently observed with the goniometer.

As an additional check, the droplet's acceleration is calculated by extracting droplet positions at a number of time-points from the video. If we assume that once droplet motion has begun any adhesive or frictional forces are absent from the droplet–surface interface, it follows that acceleration, $a = g \sin \alpha$. Under this assumption a slide angle of 1.2° is obtained. The close correspondence between this value and the direct goniometer reading provides further support for the view that a negligible number of pores are filled with water, enabling liquid–solid interactions to be extremely weak once motion begins.

3.5. Performance under condensing conditions

Measurements of droplet formation and shedding under condensing conditions show very different behavior from that of droplets introduced to the surface from above. Figures 6a and 6b are scanning electron micrographs of aluminum surfaces coated at 25 mM and 70 °C (Process A in Table 1), and at 75 mM and 110 °C, respectively. The inset photographs show 5.5 μL water droplets with sessile contact angles of 174° and 178° on the respective surfaces. Although the 75 mM/110 °C surface offers the highest sessile water contact angle and lowest hysteresis of all process conditions explored (Figure 2a–b), this surface does not perform optimally when exposed to air with supersaturation $S = 1.50^{+0.20}_{-0.15}$ (see SI for calculation of S). After ten minutes at these conditions, large droplets with contact angles $\ll 178°$ have formed and pinned to the surface. In contrast, the surface made by Process A (25 mM/70 °C) shows far better condensing performance, with condensate maintaining a higher contact angle (albeit still less than 178°) and shedding from the surface into the air flow at droplet diameters well below 1 mm. We do not observe coalescence-induced droplet jumping but we do see a sustained droplet-shedding process under the action of the 10 ms^{-1} air flow, and at a much higher supersaturation than the 1.12 flooding threshold reported by Mijkovic [4].

One plausible explanation for Process A's superior condensing performance yet non-optimal sessile droplet water contact angle is that the different processes yield pore sidewall profiles that vary with depth in different ways. Condensing droplets nucleate throughout the pores and then, for dropwise shedding, need to be expelled from the pores, whereas sessile water droplets only encounter the tips of most pores, penetrating only the few pores that occupy the least re-entrant tail of the sidewall angle distribution. It is possible therefore that Process A (Figure 6a) produces less strongly re-entrant pore *tips* than the 75 mM/110 °C process (Figure 6b), but, on average, more re-entrant profiles *beneath* the tips. If this is indeed the case, it would explain why surfaces made with Process A would be the more effective at expelling condensate.

This explanation is consistent with the finding from Figure 4a that Process A delivers higher sessile contact angles for a *range* of liquids than surfaces produced at higher reactant concentration (Process C) or higher temperature (Process B). Sessile droplet characterization with a range of liquids, including lower-surface-tension liquids that penetrate and probe a larger fraction of the surface's pores, are expected to yield more information about the structure deep inside the pores and therefore to offer a better indication of how well a surface will shed condensing droplets than characterizing it only with water.

It is interesting to note that the value of E^*, as defined in Equation 1, is well below 1 for processes A–C (Table 1). Calculation of E^* is based here on an assumption of $\theta_0 = 119°$ as reported by Wang [76]. Although we did not extract a value for r for the 75 mM/110 °C surface in Figure 6b and 6d, and so cannot directly estimate E^* for this surface, it is reasonable to suppose that its E^* will be very close to that of processes A–C, for which E^* lies in the tight range of 0.13–0.14. Enright's model suggests that partial wetting occurs for $E^* < 1$, and yet we observe flooding of the 75 mM/110 °C surface, implying the

Wenzel mode. Thus, richer surface characterization of the kinds we demonstrate above may well be needed to predict whether dropwise condensation will be successful.

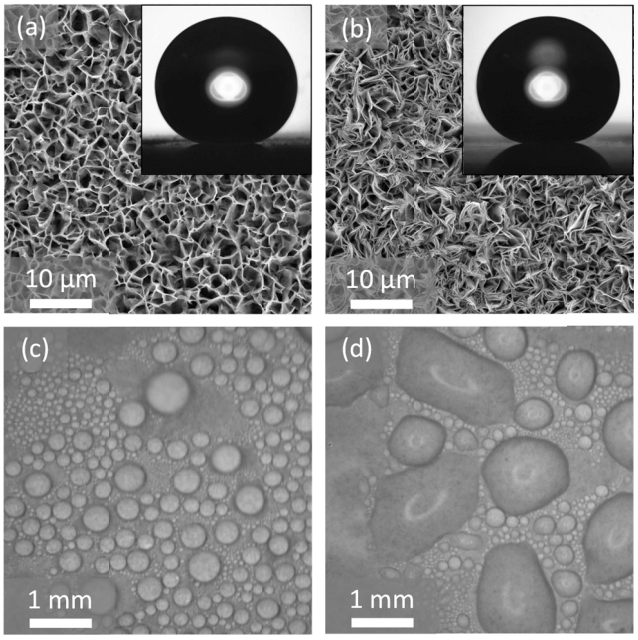

Figure 6. Scanning electron micrographs of aluminum surfaces coated at (a) 25 mM and 70 °C and (b) 75 mM and 110 °C. The insets are photographs of 5.5 μL droplets (diameter ≈ 2.1 mm) with contact angles of (a) 174° and (b) 178°. Images of the samples after 10 minutes in air at a water supersaturation of $1.50^{+0.20}_{-0.15}$ and an air velocity of 10±0.25 m/s for the same samples synthesized at (c) 70 °C and (d) 110 °C indicate significantly different properties. The surface at 70 °C maintains dropwise condensation and shedding while the surface synthesized at 110 °C floods.

4. Concluding remarks

- ZnO has been hydrothermally synthesized on aluminum and covalently terminated with a fluorosilane molecule to produce a surface that exhibits sustained dropwise condensation of water from air at supersaturations of at least ~1.5.
- Droplets detach from the produced surfaces at diameters less than 1 mm in a flowing air stream with an average velocity of 10 ms^{-1}. There thus appears to be considerable scope to use the ZnO coating to enhance heat transfer and maintain dry surfaces on the air-side of cooling coils.
- The key to the droplet-shedding superhydrophobicity appears to lie in the creation of sub-micrometer, re-entrant pore geometries. The more strongly re-entrant the pores are on average, the more comprehensively repellent a surface tends to be to liquids with a range of surface tensions.
- The maximum sessile water contact angle (178˚), minimum hysteresis (3˚) and minimum roll-off angle (1˚) that we have achieved with growth conditions of 75 mM, 110 ˚C and 90 min are superior to all other reports we have seen for aluminum superhydrophobic modification.
- Meanwhile, a set of optimal processing conditions for promoting dropwise condensation at atmospheric pressure appears to be 25 mM, 70 °C and 90 min. Unexpectedly, these conditions are different from those that give the maximal sessile water contact angle and minimal hysteresis. We attribute this contrast to a difference between the sidewall re-entrant characteristics at the tips of the pores and the characteristics deeper inside the pores.

- Because this new material is grown by simple immersion in an aqueous bath at atmospheric pressure, we anticipate that it will be quite feasible to combine this process with prior patterning of the target surface at length-scales larger than the synthesized pores — for example by mechanically embossing microstructures into an aluminum surface. Such an approach may enable even higher performance at low cost by mimicking natural multi-scale structures.
- The identification of process parameters that yield reliably dropwise-condensing surfaces, as reported here, is an important step towards being able to engineer more effective air-side heat transfer. Full characterization of these surfaces will of course require measurements of their condensation heat transfer coefficients. These measurements are the subject of ongoing work to be reported in a future publication.

Acknowledgements

The authors thank the staff of the UC Berkeley Biomolecular Nanotechnology Center (BNC) for assistance, and gratefully acknowledge the assistance of John Madura in constructing the condensation test apparatus. This work was supported by the Singapore–Berkeley Building Efficiency and Sustainability in the Tropics (SinBerBEST) program, funded by the National Research Foundation, Prime Minister's Office, Singapore. The authors declare a financial interest in Nelumbo Inc.

References

[1] J. W. Rose, "Dropwise condensation theory and experiment: A review," *Proc. Inst. Mech. Eng. Part J. Power Energy*, vol. 216, no. 2, pp. 115–128, Mar. 2002.
[2] X. Ma, S. Wang, Z. Lan, B. Peng, H. B. Ma, and P. Cheng, "Wetting Mode Evolution of Steam Dropwise Condensation on Superhydrophobic Surface in the Presence of Noncondensable Gas," *J. Heat Transf.*, vol. 134, no. 2, pp. 021501–021501, Dec. 2011.
[3] N. Miljkovic, R. Enright, and E. N. Wang, "Modeling and Optimization of Superhydrophobic Condensation," *J. Heat Transf.*, vol. 135, no. 11, p. 111004, Sep. 2013.
[4] N. Miljkovic *et al.*, "Jumping-Droplet-Enhanced Condensation on Scalable Superhydrophobic Nanostructured Surfaces," *Nano Lett.*, vol. 13, no. 1, pp. 179–187, Jan. 2013.
[5] A. D. Sommers, R. Yu, N. C. Okamoto, and K. Upadhyayula, "Condensate drainage performance of a plain fin-and-tube heat exchanger constructed from anisotropic micro-grooved fins," *Int. J. Refrig.*, vol. 35, no. 6, pp. 1766–1778, Sep. 2012.
[6] C.-H. Xue, S.-T. Jia, J. Zhang, and J.-Z. Ma, "Large-area fabrication of superhydrophobic surfaces for practical applications: an overview," *Sci. Technol. Adv. Mater.*, vol. 11, no. 3, p. 033002, Feb. 2010.
[7] N. Miljkovic, R. Enright, and E. N. Wang, "Effect of Droplet Morphology on Growth Dynamics and Heat Transfer during Condensation on Superhydrophobic Nanostructured Surfaces," *ACS Nano*, vol. 6, no. 2, pp. 1776–1785, Feb. 2012.
[8] R. Enright, N. Miljkovic, A. Al-Obeidi, C. V. Thompson, and E. N. Wang, "Condensation on Superhydrophobic Surfaces: The Role of Local Energy Barriers and Structure Length Scale," *Langmuir*, vol. 28, no. 40, pp. 14424–14432, Oct. 2012.
[9] K. Rykaczewski *et al.*, "How nanorough is rough enough to make a surface superhydrophobic during water condensation?," *Soft Matter*, vol. 8, no. 33, pp. 8786–8794, Aug. 2012.
[10] A. Lafuma and D. Quéré, "Superhydrophobic states," *Nat. Mater.*, vol. 2, no. 7, pp. 457–460, Jul. 2003.
[11] R. D. Narhe and D. A. Beysens, "Growth Dynamics of Water Drops on a Square-Pattern Rough Hydrophobic Surface," *Langmuir*, vol. 23, no. 12, pp. 6486–6489, Jun. 2007.
[12] C. Dorrer and J. Rühe, "Condensation and Wetting Transitions on Microstructured Ultrahydrophobic Surfaces," *Langmuir*, vol. 23, no. 7, pp. 3820–3824, Mar. 2007.

[13] K. A. Wier and T. J. McCarthy, “Condensation on Ultrahydrophobic Surfaces and Its Effect on Droplet Mobility: Ultrahydrophobic Surfaces Are Not Always Water Repellant,” *Langmuir*, vol. 22, no. 6, pp. 2433–2436, Mar. 2006.
[14] C.-H. Chen *et al.*, “Dropwise condensation on superhydrophobic surfaces with two-tier roughness,” *Appl. Phys. Lett.*, vol. 90, no. 17, p. 173108, Apr. 2007.
[15] “Air Conditioning | Department of Energy.” [Online]. Available: http://www.energy.gov/energysaver/air-conditioning. [Accessed: 21-Nov-2016].
[16] K. J. Chua, S. K. Chou, W. M. Yang, and J. Yan, “Achieving better energy-efficient air conditioning – A review of technologies and strategies,” *Appl. Energy*, vol. 104, pp. 87–104, Apr. 2013.
[17] T. Hiroaki and T. Takaharu, “A microscopic study of dropwise condensation,” *Int. J. Heat Mass Transf.*, vol. 27, no. 3, pp. 327–335, Mar. 1984.
[18] Liping Liu and A. M. Jacobi, “The Impact of Fin Surface Wettability on the Performance of Dehumidifying Heat Exchangers,” *ASHRAE Trans.*, vol. 120, no. 1, pp. 1–8, Jan. 2014.
[19] G. Gratzl, C. Paulik, and M. Lackner, “Antimicrobial Surfaces,” in *Kirk-Othmer Encyclopedia of Chemical Technology*, John Wiley & Sons, Inc., 2000.
[20] A. D. Sommers, J. Ying, and K. F. Eid, “Predicting the onset of condensate droplet departure from a vertical surface due to air flow—Applications to topographically-modified, micro-grooved surfaces,” *Exp. Therm. Fluid Sci.*, vol. 40, pp. 38–49, Jul. 2012.
[21] R. Enright, N. Miljkovic, J. Sprittles, K. Nolan, R. Mitchell, and E. N. Wang, “How Coalescing Droplets Jump,” *ACS Nano*, vol. 8, no. 10, pp. 10352–10362, Oct. 2014.
[22] R. N. Wenzel, “Resistance of Solid Surfaces to Wetting by Water,” *Ind. Eng. Chem.*, vol. 28, no. 8, pp. 988–994, Aug. 1936.
[23] A. B. D. Cassie and S. Baxter, “Wettability of porous surfaces,” *Trans. Faraday Soc.*, vol. 40, no. 0, pp. 546–551, Jan. 1944.
[24] N. Miljkovic and E. N. Wang, “Condensation heat transfer on superhydrophobic surfaces,” *MRS Bull.*, vol. 38, no. 05, pp. 397–406, May 2013.
[25] K. K. Varanasi, M. Hsu, N. Bhate, W. Yang, and T. Deng, “Spatial control in the heterogeneous nucleation of water,” *Appl. Phys. Lett.*, vol. 95, no. 9, pp. 094101-094101-3, 2009.
[26] R. Enright, N. Miljkovic, N. Dou, Y. Nam, and E. N. Wang, “Condensation on Superhydrophobic Copper Oxide Nanostructures,” *J. Heat Transf.*, vol. 135, no. 9, pp. 091304–091304, Jul. 2013.
[27] A. Ahuja *et al.*, “Nanonails: A Simple Geometrical Approach to Electrically Tunable Superlyophobic Surfaces,” *Langmuir*, vol. 24, no. 1, pp. 9–14, Jan. 2008.
[28] C.-H. Choi, U. Ulmanella, J. Kim, C.-M. Ho, and C.-J. Kim, “Effective slip and friction reduction in nanograted superhydrophobic microchannels,” *Phys. Fluids 1994-Present*, vol. 18, no. 8, p. 087105, Aug. 2006.
[29] E. Martines, K. Seunarine, H. Morgan, N. Gadegaard, C. D. W. Wilkinson, and M. O. Riehle, “Superhydrophobicity and Superhydrophilicity of Regular Nanopatterns,” *Nano Lett.*, vol. 5, no. 10, pp. 2097–2103, 2005.
[30] B. Lu and W. J. Meng, “Roll Molding of Microchannel Arrays on Al and Cu Sheet Metals: A Method for High-Throughput Manufacturing,” *J. Micro Nano-Manuf.*, vol. 2, no. 1, pp. 011007–011007, Dec. 2013.
[31] L. Liu, A. M. Jacobi, and D. Chvedov, “A surface embossing technique to create micro-grooves on an aluminum fin stock for drainage enhancement,” *J. Micromechanics Microengineering*, vol. 19, no. 3, p. 035026, 2009.
[32] J. Hasan and K. Chatterjee, “Recent advances in engineering topography mediated antibacterial surfaces,” *Nanoscale*, vol. 7, no. 38, pp. 15568–15575, Sep. 2015.
[33] L. Brockway and H. Taylor, “A statistical model for the wettability of surfaces with heterogeneous pore geometries,” *Mater. Res. Express*, vol. 3, no. 10, p. 105039, 2016.
[34] A. Tuteja *et al.*, “Designing Superoleophobic Surfaces,” *Science*, vol. 318, no. 5856, pp. 1618–1622, Dec. 2007.

[35] T. “Leo” Liu and C.-J. “CJ” Kim, “Turning a surface superrepellent even to completely wetting liquids,” *Science*, vol. 346, no. 6213, pp. 1096–1100, Nov. 2014.
[36] S. S. Chhatre *et al.*, “Scale Dependence of Omniphobic Mesh Surfaces,” *Langmuir*, vol. 26, no. 6, pp. 4027–4035, Mar. 2010.
[37] M. He *et al.*, “Hierarchical Porous Surface for Efficiently Controlling Microdroplets’ Self-Removal,” *Adv. Mater.*, vol. 25, no. 16, pp. 2291–2295, Apr. 2013.
[38] Z. Guo, F. Zhou, J. Hao, and W. Liu, “Stable Biomimetic Super-Hydrophobic Engineering Materials,” *J. Am. Chem. Soc.*, vol. 127, no. 45, pp. 15670–15671, Nov. 2005.
[39] I. Bernagozzi, C. Antonini, F. Villa, and M. Marengo, “Fabricating superhydrophobic aluminum: An optimized one-step wet synthesis using fluoroalkyl silane,” *Colloids Surf. Physicochem. Eng. Asp.*, vol. 441, no. 10.1016/j.colsurfa.2013.05.042, pp. 919–924, Jan. 2014.
[40] N. Saleema, D. K. Sarkar, R. W. Paynter, and X.-G. Chen, “Superhydrophobic Aluminum Alloy Surfaces by a Novel One-Step Process,” *ACS Appl. Mater. Interfaces*, vol. 2, no. 9, pp. 2500–2502, Sep. 2010.
[41] A. M. Md Jani, D. Losic, and N. H. Voelcker, “Nanoporous anodic aluminium oxide: Advances in surface engineering and emerging applications,” *Prog. Mater. Sci.*, vol. 58, no. 5, pp. 636–704, Jun. 2013.
[42] Y. Kim, S. Lee, H. Cho, B. Park, D. Kim, and W. Hwang, “Robust Superhydrophilic/Hydrophobic Surface Based on Self-Aggregated Al2O3 Nanowires by Single-Step Anodization and Self-Assembly Method,” *ACS Appl. Mater. Interfaces*, vol. 4, no. 10, pp. 5074–5078, Oct. 2012.
[43] B. Yin *et al.*, “Novel strategy in increasing stability and corrosion resistance for super-hydrophobic coating on aluminum alloy surfaces,” *Appl. Surf. Sci.*, vol. 258, no. 1, pp. 580–585, Oct. 2011.
[44] E. Jenner, C. Barbier, and B. D’Urso, “Durability of hydrophobic coatings for superhydrophobic aluminum oxide,” *Appl. Surf. Sci.*, vol. 282, pp. 73–76, Oct. 2013.
[45] M. Song, Y. Liu, S. Cui, L. Liu, and M. Yang, “Fabrication and icing property of superhydrophilic and superhydrophobic aluminum surfaces derived from anodizing aluminum foil in a sodium chloride aqueous solution,” *Appl. Surf. Sci.*, vol. 283, pp. 19–24, Oct. 2013.
[46] F. Hizal, N. Rungraeng, S. Jun, and C. H. Choi, “Nano-engineered alumina surfaces for prevention of bacteria adhesions,” in *2014 9th IEEE International Conference on Nano/Micro Engineered and Molecular Systems (NEMS)*, 2014, pp. 17–22.
[47] L. Brockway, V. Vasiraju, M. K. Sunkara, and S. Vaddiraju, “Engineering Efficient Thermoelectrics from Large-Scale Assemblies of Doped ZnO Nanowires: Nanoscale Effects and Resonant-Level Scattering,” *ACS Appl. Mater. Interfaces*, vol. 6, no. 17, pp. 14923–14930, Sep. 2014.
[48] J. Alvarez-Quintana, E. Martínez, E. Pérez-Tijerina, S. A. Pérez-García, and J. Rodríguez-Viejo, “Temperature dependent thermal conductivity of polycrystalline ZnO films,” *J. Appl. Phys.*, vol. 107, no. 6, p. 063713, Mar. 2010.
[49] L. E. Greene *et al.*, “General Route to Vertical ZnO Nanowire Arrays Using Textured ZnO Seeds,” *Nano Lett.*, vol. 5, no. 7, pp. 1231–1236, Jul. 2005.
[50] B.-B. Wang, J.-T. Feng, Y.-P. Zhao, and T. X. Yu, “Fabrication of Novel Superhydrophobic Surfaces and Water Droplet Bouncing Behavior — Part 1: Stable ZnO–PDMS Superhydrophobic Surface with Low Hysteresis Constructed Using ZnO Nanoparticles,” *J. Adhes. Sci. Technol.*, vol. 24, no. 15–16, pp. 2693–2705, Jan. 2010.
[51] X. L. Hu, Y. Masuda, T. Ohji, and K. Kato, “Rapid Low-Temperature Synthesis of Porous ZnO Nanoparticle Film by Self-Hydrolysis Technique,” *Key Eng. Mater.*, vol. 445, pp. 123–126, 2010.
[52] X. Wu, L. Zheng, and D. Wu, “Fabrication of Superhydrophobic Surfaces from Microstructured ZnO-Based Surfaces via a Wet-Chemical Route,” *Langmuir*, vol. 21, no. 7, pp. 2665–2667, Mar. 2005.
[53] L. Yao, M. Zheng, C. Li, L. Ma, and W. Shen, “Facile synthesis of superhydrophobic surface of ZnO nanoflakes: chemical coating and UV-induced wettability conversion,” *Nanoscale Res. Lett.*, vol. 7, no. 1, p. 216, Apr. 2012.

[54] N. L. Tarwal and P. S. Patil, “Superhydrophobic and transparent ZnO thin films synthesized by spray pyrolysis technique,” *Appl. Surf. Sci.*, vol. 256, no. 24, pp. 7451–7456, Oct. 2010.
[55] Y. Lu, S. Sathasivam, J. Song, C. R. Crick, C. J. Carmalt, and I. P. Parkin, “Robust self-cleaning surfaces that function when exposed to either air or oil,” *Science*, vol. 347, no. 6226, pp. 1132–1135, Mar. 2015.
[56] J. Liu, G. Aguilar, R. Munoz, and Y. Yan, “Hydrophilic zeolite coatings for improved heat transfer: A quantitative analysis,” *AIChE J.*, vol. 54, no. 3, pp. 779–790, Mar. 2008.
[57] G. Azimi, R. Dhiman, H.-M. Kwon, A. T. Paxson, and K. K. Varanasi, “Hydrophobicity of rare-earth oxide ceramics,” *Nat. Mater.*, vol. 12, no. 4, pp. 315–320, Apr. 2013.
[58] L.-Y. Meng and S.-J. Park, “Superhydrophobic carbon-based materials: a review of synthesis, structure, and applications,” *Carbon Lett.*, vol. 15, no. 2, pp. 89–104, 2014.
[59] J.-L. Liu, X.-Q. Feng, G. Wang, and S.-W. Yu, “Mechanisms of superhydrophobicity on hydrophilic substrates,” *J. Phys. Condens. Matter*, vol. 19, no. 35, p. 356002, 2007.
[60] N. Miljkovic, D. J. Preston, R. Enright, and E. N. Wang, “Electrostatic charging of jumping droplets,” *Nat. Commun.*, vol. 4, p. 2517, Sep. 2013.
[61] Y. Huang, D. K. Sarkar, D. Gallant, and X.-G. Chen, “Corrosion resistance properties of superhydrophobic copper surfaces fabricated by one-step electrochemical modification process,” *Appl. Surf. Sci.*, vol. 282, pp. 689–694, Oct. 2013.
[62] M. Ma, R. M. Hill, J. L. Lowery, S. V. Fridrikh, and G. C. Rutledge, “Electrospun Poly(Styrene-block-dimethylsiloxane) Block Copolymer Fibers Exhibiting Superhydrophobicity,” *Langmuir*, vol. 21, no. 12, pp. 5549–5554, Jun. 2005.
[63] L. Feng *et al.*, “Creation of a Superhydrophobic Surface from an Amphiphilic Polymer,” *Angew. Chem.*, vol. 115, no. 7, pp. 824–826, Feb. 2003.
[64] H. Y. Erbil, A. L. Demirel, Y. Avcı, and O. Mert, “Transformation of a Simple Plastic into a Superhydrophobic Surface,” *Science*, vol. 299, no. 5611, pp. 1377–1380, Feb. 2003.
[65] H. Yabu and M. Shimomura, “Single-Step Fabrication of Transparent Superhydrophobic Porous Polymer Films,” *Chem. Mater.*, vol. 17, no. 21, pp. 5231–5234, Oct. 2005.
[66] M. J. Kreder, J. Alvarenga, P. Kim, and J. Aizenberg, “Design of anti-icing surfaces: smooth, textured or slippery?,” *Nat. Rev. Mater.*, vol. 1, p. 15003, Jan. 2016.
[67] N. A. Patankar, “Mimicking the Lotus Effect: Influence of Double Roughness Structures and Slender Pillars,” *Langmuir*, vol. 20, no. 19, pp. 8209–8213, Sep. 2004.
[68] M. He, Y. Ding, J. Chen, and Y. Song, “Spontaneous Uphill Movement and Self-Removal of Condensates on Hierarchical Tower-like Arrays,” *ACS Nano*, vol. 10, no. 10, pp. 9456–9462, Oct. 2016.
[69] A. F. Stalder, T. Melchior, M. Müller, D. Sage, T. Blu, and M. Unser, “Low-bond axisymmetric drop shape analysis for surface tension and contact angle measurements of sessile drops,” *Colloids Surf. Physicochem. Eng. Asp.*, vol. 364, no. 1–3, pp. 72–81, Jul. 2010.
[70] A. F. Stalder, G. Kulik, D. Sage, L. Barbieri, and P. Hoffmann, “A snake-based approach to accurate determination of both contact points and contact angles,” *Colloids Surf. Physicochem. Eng. Asp.*, vol. 286, no. 1–3, pp. 92–103, Sep. 2006.
[71] C. Korte and A. M. Jacobi, “Condensate Retention Effects on the Performance of Plain-Fin-and-Tube Heat Exchangers: Retention Data and Modeling,” *J. Heat Transf.*, vol. 123, no. 5, pp. 926–936, Apr. 2001.
[72] G. McHale, N. J. Shirtcliffe, and M. I. Newton, “Contact-Angle Hysteresis on Super-Hydrophobic Surfaces,” *Langmuir*, vol. 20, no. 23, pp. 10146–10149, Nov. 2004.
[73] K. S. Birdi, *Surface Chemistry Essentials*. CRC Press, 2013.
[74] G. Korosi and E. S. Kovats, “Density and surface tension of 83 organic liquids,” *J. Chem. Eng. Data*, vol. 26, no. 3, pp. 323–332, Jul. 1981.
[75] C. Lv, C. Yang, P. Hao, F. He, and Q. Zheng, “Sliding of Water Droplets on Microstructured Hydrophobic Surfaces,” *Langmuir*, vol. 26, no. 11, pp. 8704–8708, Jun. 2010.

[76] L. Wang, J. Wei, and Z. Su, “Fabrication of Surfaces with Extremely High Contact Angle Hysteresis from Polyelectrolyte Multilayer,” *Langmuir*, vol. 27, no. 24, pp. 15299–15304, Dec. 2011.

Supplementary information

A nanoporous, ultrahydrophobic aluminum-coating process with exceptional dropwise condensation and shedding properties

Lance Brockway[1,2] and Hayden Taylor[1,2,*]

[1] Department of Mechanical Engineering,
6159 Etcheverry Hall, University of California, Berkeley, CA 94720

[2] Berkeley Education Alliance for Research in Singapore (BEARS)
CREATE Tower, 1 Create Way, #11-00 Singapore 138602

*Corresponding author – telephone: +1 510 642-4901; e-mail: hkt@berkeley.edu

S1. Specifications of condensation experimental apparatus

We constructed a closed-loop wind tunnel to provide air with controlled temperature and relative humidity representative of tropical climates. Briefly, the majority of the loop, including the bends, is constructed from 150 mm-diameter galvanized steel ducting, insulated by a layer of fiberglass (Owens Corning) with an *R* value [1] of 6. The sample observation section has a 100 mm-square cross-section and is constructed from timber and ABS, with a transparent 3 mm-thick acrylic window for video imaging of the condensation process. Experimental samples are mounted with thermal grease into a machined aluminum alloy holder that is chilled with water from a VWR 1175 recirculating chiller. Air temperature is raised by a Neptronic 2 kW electric duct heater. Air is driven by a Delta Electronics THB1548AG fan with a 530 ft^3/min capacity. Humidity is raised by a Copper Head cold mist fogger that is manually controlled and injects water droplets downstream of the heater. Sensiron SHT15 humidity and temperature sensor modules (Adafruit Technologies) are positioned approximately 100 mm upstream and downstream of the experimental samples to determine the air conditions; air conditions reported in this paper were recorded from the upstream sensor module. Air velocity is sensed with a Fluke 922 anemometer placed in the observation section. The surface temperature of the sample is sensed with an Omega 3105 DIN Class "A" PT100 resistance temperature detector (RTD) surface-mount three-wire element. The fan and heater are controlled and data from the sensors are logged using a pair of Arduino Uno microcontroller boards that interface to Matlab and Simulink on a desktop computer.

S2. Computation of supersaturation at sample surface

The condensation test apparatus is instrumented to record the average dry bulb temperature, T_{air}, of the flowing air and its relative humidity (RH), S_{air}. From T_{air} we estimate the saturation vapor pressure $P_{\mathrm{ws}}(T_{\mathrm{air}})$ of water in the air, where [2]:

$$P_{\mathrm{ws}}(T) = (1000\ \mathrm{Pa}) \times \mathrm{e}^{\left[16.7 - \frac{4060}{T-37}\right]} \tag{S.1}$$

and T is defined in Kelvin. By definition, the water vapor pressure in the air, $P_{\mathrm{w}}(T_{\mathrm{air}})$, is:

$$P_{\mathrm{w}}(T_{\mathrm{air}}) = P_{\mathrm{ws}}(T_{\mathrm{air}})S_{\mathrm{air}}. \quad \text{(S.2)}$$

We assume that the water vapor pressure on the air side of the chilled surface is equal to that in the bulk of the air, $P_{\mathrm{w}}(T_{\mathrm{air}})$, because the samples are small (diameter 10 mm) compared with the size of the air duct (diameter ~100 mm) and are not expected to perturb the amount of water vapor in the air substantially. Therefore, we use Equation S.1 to re-evaluate the saturation vapor pressure for air at the temperature of the chilled sample surface, T_{surf}, and obtain the supersaturation, S, of water vapor at the chilled surface:

$$S = P_{\mathrm{w}}(T_{\mathrm{air}})/P_{\mathrm{ws}}(T_{\mathrm{surf}}) \quad \text{(S.3)}$$

Taking the air temperature to be 40 ± 0.5 ℃, the chilled surface temperature to be 15 ± 0.5 ℃, and the air's relative humidity to be $35 \pm 2\%$, we obtain $S = 1.50^{+0.20}_{-0.15}$. The upper bound of the estimated supersaturation comes from assuming an air temperature of 40.5 ℃, an air RH of 37%, and a chilled surface temperature of 14.5 ℃. The lower bound of S comes from assuming an air temperature of 39.5 ℃, an air RH of 33%, and a chilled surface temperature of 15.5 ℃.

S3. Complete contact angle and hysteresis results

Table S1. Measured water contact angles and hysteresis values, in degrees. Sessile droplet contact angle results are based on ten separate measurements per sample; advancing, receding and hysteresis values are based on five measurements per sample.

Process conditions		Sessile droplet contact angle		Advancing contact angle		Receding contact angle		Contact angle hysteresis	
Processing temperature (°C)	Zinc nitrate concentration (mM)	Mean	Std. err.	Mean	Std. err.	Mean	Std. err.	Mean	Std. err.
70	10	161.1	1.0	169.9	1.0	151.3	1.4	18.6	2.2
	25	173.2	0.5	176.3	0.7	168.6	1.6	7.7	1.2
	50	173.7	0.3	175.7	0.7	168.5	1.4	7.2	1.2
	75	169.2	0.8	174.5	0.6	161.7	1.9	12.8	2.0
	100	156.8	0.9	171.9	1.2	142.0	1.9	29.9	1.1
90	10	170.5	0.8	175.1	0.3	164.2	1.6	10.9	1.2
	25	173.0	0.7	176.5	0.7	170.5	0.9	6.1	0.6
	50	174.0	0.6	175.9	0.4	168.1	0.6	7.8	0.4
	75	176.6	0.6	176.5	0.9	170.5	0.6	6.0	0.8
	100	174.5	0.7	175.9	0.6	167.6	0.8	8.3	0.8
110	10	161.7	1.0	169.0	0.3	149.0	1.8	20.0	1.8
	25	173.9	0.6	176.6	0.3	168.8	1.0	7.8	1.2
	50	174.5	0.6	175.1	0.6	170.0	0.8	5.1	0.5
	75	177.6	0.3	176.7	0.5	174.0	0.5	2.7	0.7
	100	166.7	1.1	171.1	2.2	147.9	1.1	23.2	1.5

Table S2. Measured contact angles, in degrees, for PEGDA 700 Da. Mean and standard error of the mean are based on five separate droplet measurements per sample.

Process conditions		Sessile droplet contact angle	
Processing temperature (°C)	**Zinc nitrate concentration (mM)**	**Mean**	**Std. err.**
70	10	145.7	2.5
	25	151.5	1.5
	50	124.2	0.3
	75	112.9	1.6
	100	109.6	0.6
90	10	141.3	0.5
	25	139.8	0.4
	50	140.0	0.8
	75	133.3	0.6
	100	130.8	0.4
110	10	49.0	5.8
	25	144.8	1.2
	50	138.4	1.0
	75	135.8	1.7
	100	128.4	1.3

Table S3. Measured sessile droplet contact angles, in degrees, of water on a flat silanized surface and on three surfaces produced under specific conditions. Mean and standard error of the mean are based on five separate droplet measurements per sample. TDG = thidiglycol; PEGDA = polyethylene glycol diacrylate with molar mass of 700 g; DPG = dipropylene glycol. The surface made using Process C was completely wet by methanol, with no contact angle measurable.

Surface		**Probe liquid** [surface tension, mN/m]					
		Water [72.8]	Glycerol [64.0]	TDG [54.0]	PEGDA [42.3]	DPG [33.9]	Methanol [22.7]
Flat silicon wafer	Mean	105.3	102.9	96.6	83.5	70.2	53.2
	Std. Err.	0.2	1.6	0.5	0.7	1.0	1.0
Process A 25 mM, 70 ˚C	Mean	173.8	169.6	162.7	151.5	123.7	62.3
	Std. Err.	0.8	0.5	0.6	1.5	0.8	1.7
Process B 50 mM, 110 ˚C	Mean	174.4	167.3	159.4	138.4	105.4	42.0
	Std. Err.	0.4	0.4	0.4	1.0	1.7	3.1
Process C 100 mM, 70 ˚C	Mean	157.0	148.2	133.0	109.6	Not measured	Completely wet surface
	Std. Err.	1.5	1.1	1.8	0.6		

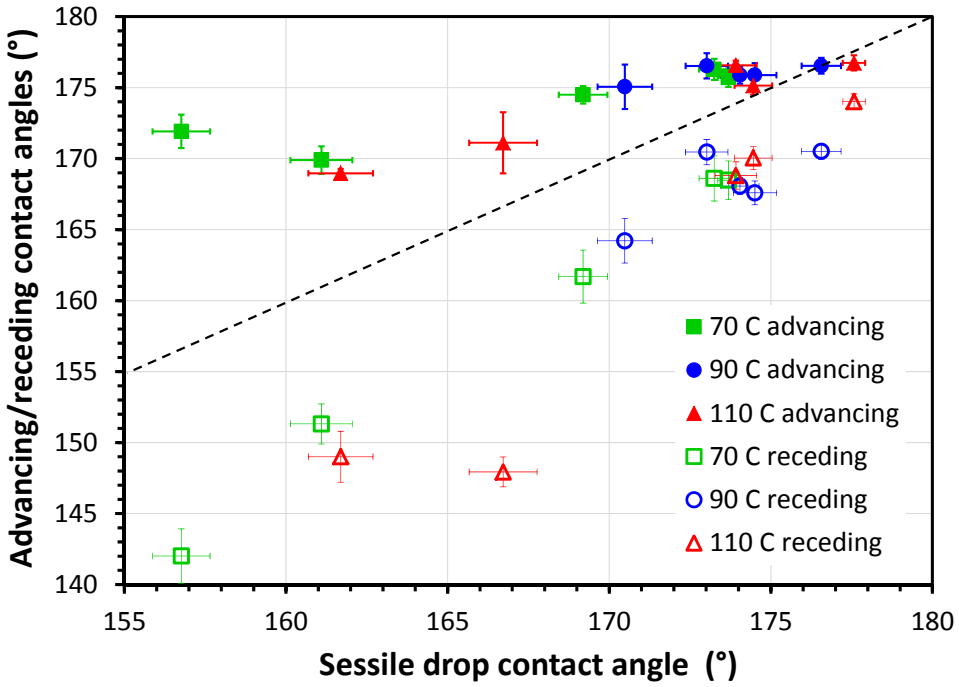

Figure S1. Advancing and receding water contact angles against sessile drop contact angle. Error bars show ± one standard error of the mean, based on five measurements for advancing and receding contact angles and ten measurements for sessile droplet contact angle. The dashed line indicates values for which sessile droplet contact angle would equal the advancing/receding contact angle. For a given surface formation process, the difference between the advancing and sessile droplet contact angles tends to be smaller than that between the sessile droplet and receding angles.

S4. Comparison of hysteresis results with the model of McHale et al. [3]

McHale proposes a model for predicting the hysteresis of a rough surface, $\Delta\theta_e^{\mathrm{W,CB}}$ given the hysteresis of a flat surface with the same chemistry, $\Delta\theta_e^{\mathrm{min}}$. The model considers both the Wenzel wetting mode, in which the predicted hysteresis increases with roughness, and the Cassie-Baxter composite mode, in which the predicted hysteresis decreases as the solid fraction of the interface reduces, while apparent sessile contact angle increases. Since our results indicate that the hysteresis of our ZnO-based coating decreases with increasing apparent contact angle, we consider the correspondence between our results and McHale's model for Cassie-Baxter interfaces.

McHale supposes that for the contact line to begin moving, a minimum change in surface free energy, ΔF_{min}, must be imparted to a droplet. Considering a *flat* surface with a particular apparent sessile contact angle, θ_0, the required change in surface free energy is assumed to be related to the change in contact angle by:

$$\Delta\theta_0^{\mathrm{min}} = \left(\frac{\partial F}{\partial \theta}\right)^{-1}_{\theta=\theta_0} \Delta F_{\mathrm{min}}. \qquad \text{(S.4)}$$

For a Cassie-Baxter interface, the required change in apparent contact angle is assumed to be reduced by the gain factor, $G(\phi_T, \theta_0)$, which is the sensitivity of the Cassie-Baxter contact angle, θ^*, to changes in the contact angle on a flat surface:

$$\Delta\theta^* > G(\phi_T, \theta_0)\left(\frac{\partial \mathrm{F}}{\partial \theta}\right)^{-1}_{\theta=\theta_0} \Delta \mathrm{F}_{\min} = G(\phi_T, \theta_0)\Delta\theta_0^{\min} \tag{S.5}$$

where $G(\phi_T, \theta_0)$ is found via differentiation of the Cassie-Baxter relationship:

$$G(\phi_T, \theta_0) = \frac{\mathrm{d}\theta^*}{\mathrm{d}\theta_0} = \frac{\phi_T \sin\theta_0}{\sqrt{1-[-1+\phi_T(\cos\theta_0+1)]^2}}. \tag{S.6}$$

In Figure 2c we show the predictions of McHale's model as a dashed line. For each value of observed sessile contact angle, we estimate ϕ_T using the relationship from our earlier work on the modeling of porous surfaces [4]:

$$\phi_T \approx \frac{\cos\theta^* + 1}{\cos\theta_0 + 1} \tag{S.7}$$

The value of θ_0 is taken as 105°, based on our measurements on a silanized silicon surface, and $\Delta\theta_0^{\min}$ (hysteresis on a flat surface) is taken to be 20°, based on the report of Wang [5]. We then find McHale's prediction of the minimum hysteresis for each apparent sessile contact angle using equations S.5 and S.6. The hysteresis is the difference between advancing and receding contact angles and thus is assumed to equal $2\Delta\theta^*$, since $\Delta\theta^*$ is the minimum change of apparent contact angle needed to move from a sessile state into a state of either advancing *or* receding motion.

Our experimental results indicate hysteresis values that are around 2.5 times higher than the lower bound predicted by McHale's model. This substantial difference may indicate that the pores of the surfaces are not all free of water; even a few filled pores could increase the resistance to motion of a droplet. Moreover, the top surface of the material, represented by the solid area fraction ϕ_T, is not perfectly flat and this surface roughness may add to the resistance to droplet motion. Alternatively, the discrepancy could indicate that our $\Delta\theta_0^{\min}$ is substantially greater than that measured by Wang.

S5. Calculation of contact line radius

As in Lv [6], the relationship between apparent contact angle θ^* and contact line radius R is:

$$R = \left[\frac{3V}{\pi(2 - 3\cos\theta^* + \cos^3\theta^*)}\right]^{\frac{1}{3}} \sin\theta^* \tag{S.8}$$

where V is the volume of the droplet.

S6. X-ray diffraction characterization of zinc oxide film

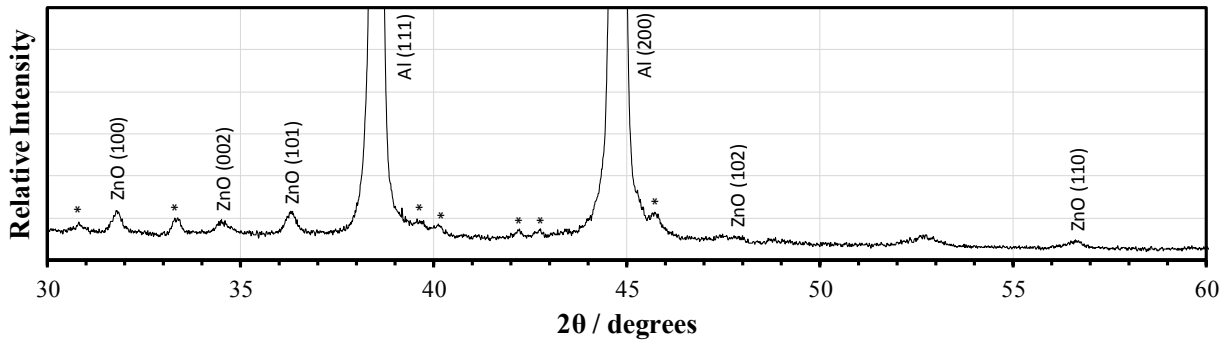

Figure S2. XRD spectrograph of the porous zinc oxide film grown on an aluminum substrate at 25 mM reactant concentrations and 70 °C (Process A). The zinc oxide peaks along with those of the aluminum substrate are indexed and labeled. The * represent peaks that can be attributed to zinc hydroxy nitrates. These zinc hydroxy nitrates are likely to represent residual, incompletely reacted materials on the sample surface. The angle θ is that between the plane of the sample and the incident beam.

References

[1] "Insulation | Department of Energy." [Online]. Available: http://energy.gov/energysaver/insulation. [Accessed: 15-Dec-2016].

[2] D. Rim, S. Schiavon, and W. W. Nazaroff, "Energy and Cost Associated with Ventilating Office Buildings in a Tropical Climate," *PLOS ONE*, vol. 10, no. 3, p. e0122310, Mar. 2015.

[3] G. McHale, N. J. Shirtcliffe, and M. I. Newton, "Contact-Angle Hysteresis on Super-Hydrophobic Surfaces," *Langmuir*, vol. 20, no. 23, pp. 10146–10149, Nov. 2004.

[4] L. Brockway and H. Taylor, "A statistical model for the wettability of surfaces with heterogeneous pore geometries," *Mater. Res. Express*, vol. 3, no. 10, p. 105039, 2016.

[5] A. Biswas, I. S. Bayer, A. S. Biris, T. Wang, E. Dervishi, and F. Faupel, "Advances in top–down and bottom–up surface nanofabrication: Techniques, applications & future prospects," *Adv. Colloid Interface Sci.*, vol. 170, no. 1–2, pp. 2–27, Jan. 2012.

[6] C. Lv, C. Yang, P. Hao, F. He, and Q. Zheng, "Sliding of Water Droplets on Microstructured Hydrophobic Surfaces," *Langmuir*, vol. 26, no. 11, pp. 8704–8708, Jun. 2010.